Title

Molybdenum Polysulfide Chalcogels as High-Capacity, Anion-Redox-Driven Electrode Materials for Li-Ion Batteries

Journal

Chemistry of Materials, 28(22)

ISSN

0897-4756 1520-5002

Authors

Doan-Nguyen, Vicky V. T
Subrahmanyam, Kota S
Butala, Megan M
et al.

Publication Date

2016-11-22

DOI

10.1021/acs.chemmater.6b03656

Peer reviewed

Molybdenum Polysulfide Chalcogels as High-Capacity, Anion-Redox-Driven Electrode Materials for Li–Ion Batteries

Vicky V. T. Doan-Nguyen,[*,†,‡] Kota S. Subrahmanyam,[¶] Megan M. Butala,[§] Jeffrey A. Gerbec,[∥] Saiful M. Islam,[¶] Katherine N. Kanipe,[⊥] Catrina E. Wilson,[⊥] Mahalingam Balasubramanian,[#] Kamila M. Wiaderek,[#] Olaf J. Borkiewicz,[#] Karena W. Chapman,[#] Peter J. Chupas,[#] Martin Moskovits,[⊥] Bruce S. Dunn,[@] Mercouri G. Kanatzidis,[¶] and Ram Seshadri[‡,§,⊥]

†*California NanoSystems Institute, University of California, Santa Barbara, CA 93106*

‡*Materials Research Laboratory, University of California, Santa Barbara, CA 93106*

¶*Department of Chemistry, Northwestern University, Evanston, IL 60208*

§*Materials Department, University of California, Santa Barbara, CA 93106*

∥*Mitsubishi Chemical Center for Advanced Materials, Santa Barbara, CA 93106*

⊥*Department of Chemistry and Biochemistry, University of California, Santa Barbara, CA 93106*

#*X-ray Science Division, Advanced Photon Source, Argonne National Laboratory, Argonne, IL 60439*

@*Department of Materials Science and Engineering, University of California, Los Angeles, CA 90095*

E-mail: vdn@mrl.ucsb.edu

Abstract

Sulfur cathodes in conversion reaction batteries offer high gravimetric capacity but suffer from parasitic polysulfide shuttling. We demonstrate here that transition metal chalcogels of approximate formula $MoS_{3.4}$ achieve high gravimetric capacity close to 600 mAh g^{-1} (close to 1000 mAh g^{-1} on a sulfur-basis), as electrode materials for lithium-ion batteries. Transition metal chalcogels are amorphous, and comprise polysulfide chains connected by inorganic linkers. The linkers appear to act as a "glue" in the electrode to prevent polysulfide shuttling. The Mo chalcogels function as electrodes in carbonate– as well as ether–based electrolytes, which further provides evidence for polysulfide solubility not being a limiting issue. We employ X-ray spectroscopy and *operando* pair distribution function techniques to elucidate the structural evolution of the electrode. Raman and X-ray photoelectron spectroscopy track the chemical moieties that arise during the anion-redox-driven processes. We find the redox state of Mo remains unchanged across the electrochemical cycling and correspondingly, the redox is anion–driven.

Introduction

Conversion-based lithium ion (Li–ion) batteries provide a higher gravimetric capacity alternative to intercalation-based mechanisms, which are limited to extraction and insertion of $<$0.6 moles of Li ions from metal oxide host lattices.[1–4] Li–sulfur (Li–S) is the most extenstively studied electrochemical couple in the conversion class. In a typical cell, the Li anode is separated from a composite cathode of sulfur, conductive carbon, and polymeric binder. The active material, sulfur, is reduced to lithium sulfide upon discharge. The theoretical gravimetric capacity of the Li–S couple is 1672 mAh g^{-1}, which makes it a highly attractive alternative to Li–ion. Li–S gravimetric capacity is quickly diminished to less than half of the initial capacity by the 10^{th} cycle,[5] which has resulted in a variety of strategies to address the technical challenges arising from the insulating nature of elemental sulfur,[6]

the volume changes upon cycling,[7] and the polysulfide shuttle involving diffusion of Li_nS_x through the bulk electrolyte.[8–13]

We have studied the use of amorphous transition metal polysulfides (chalcogels) as the active material in an electrode to overcome the poor kinetics of lithium diffusion and to prevent polysulfide shuttling experienced in Li–S batteries. Transition metal nitrides, oxides, fluorides, phosphides, and sulfides have been investigated as alternatives to S electrodes.[2] More specifically, transition metal sulfide (Cr,[14] Mn,[15] Fe,[16] Ni,[17] Cu[18]) and disulfide (Fe,[19] Co,[20] Ni,[21] Mo,[22] , and W[23]) systems have been studied due their high theoretical gravimetric capacity, which have been demonstrated to achieve between 900 mAh g^{-1} and 1300 mAh g^{-1} upon the first discharge.[24] More recently, transition metal tri– and tetrasulfide materials have been studied for their more complex chemistries as electrodes in conversion reactions involving both redox–active cationic and anionic species.[25–27] For example, upon lithiation of VS_4, the vanadium species is oxidized from V^{+4} (VS_4) to V^{+5} (Li_3VS_4) then to a mixture of both valences ($Li_{3+x}VS_4$) before reduction to V^0 (Li_2S + V).[27] This was concomitant with a reduction of the sulfur species from S_2^{2-} to S^{2-}. Despite initial high gravimetric capacities, retention remains a challenge with transitional metal sulfide electrodes. Transition metal sulfide electrodes have cation–driven redox in which the oxidation states change upon discharge and charge.[28] In the case of transition metal chalcogels, redox is anion–driven. We demonstrate here, for the first time, that sulfur in the polysulfide chains is reduced upon discharge and oxidized upon charge while Mo maintains a +4 oxidation state.

The implementation of transition metal linkers allows for the use of carbonate–based electrolytes, which is not compatible with traditional Li–S batteries. The Li-S system requires ether-based electrolytes, which enable cycling, but also cause polysulfide shuttling. Previous studies on pyrites[29] and MS_y (M = Co, Ni, Cu)[30] have demonstrated low solubilities of transition metal sulfides in carbonate–based electrolytes. Linking the polysulfide chains with inorganic linkers such as those in chalcogels provides a strategy for stabilizing

the electrode material structurally while suppressing the dissolution of lithium polysulfides.

The morphology and size dimension of the electrode material have been heavily studied to take advantage of increased surface areas for lithium diffusion in materials that operate *via* intercalation.[31,32] For molybdenum sulfide-based materials, nanotubes,[33] nanobowls,[34] nanosheets,[35] nanowires,[36] and nanoflakes,[37,38] and hollow morphologies[39] have been studied to increase electrode/electrolyte interaction, shorten the diffusion distance of Li ions, and decrease the volume changes. Often, there is a spectacular morphology evolution between the as-prepared electrode and the discharged products. The use of chalcogels is advantageous because the as-prepared active material is amorphous,[40,41] which avoids the issue of large volume changes from cycling. The porous, amorphous network of chalcogels have been demonstrated to be catalysts for hydrodesulfurization,[42] CO_2[43] adsorption, removal of radioactive iodine[44] and heavy metals such as Pb[40] and Hg,[45] and hydrogen evolution.[46,47] Here, we demonstrate that porous, amorphous network of molybdenum polysulfide chalcogels perform well as high-capacity, anion-redox driven Li–ion cathode materials. We use a combination of X-ray spectroscopy and scattering techniques to elucidate structural evolution of the electrode and understand the stability of the cathode in both carbonate-based and ether-based electrolytes.

Materials and Methods

Sol-Rite™ (1 M $LiPF_6$ in ethylene carbonate (EC): ethylmethylcarbonate (EMC) (3:7 v/v)) was provided by Mitsubishi Chemical Corporation. Bis(trifluoromethane)sulfonimide lithium salt (LiTFSI) was purchased from Alfa Aesar. Ethylene carbonate (EC), dimethyl carbonate (EC), 1,3-dioxolane (DOL), and dimethoxyethane (DME) were purchased from Sigma Aldrich. Super P® was obtained from Timcal. The synthesis of molybdenum polysulfides (MoS_x) has been reported by Subrahmanyam *et al.*[48]

X-ray diffraction (XRD) was performed in reflection mode using a PANalytical

Empyrean with a Cu Kα source. Transmission electron microscopy (TEM) was performed using a FEI T20 with a 200 kV operating voltage. Powders were sonicated in ethanol and dropcast onto a 300-mesh carbon-coated copper grid. Raman spectroscopy was performed using a Horiba Jobin-Yvon Lab ARAMIS instrument at 3.91 mW with a 633 nm laser equipped with a 50x objective lens. The powder samples were measured using a 400 μm aperture, 250 μm slit, and 1200 gratings per mm, with exposure time of 2 s, averaged 10 times. X-ray photoelectron spectroscopy (XPS) was performed using a Kratos Axis Ultra with a monochromatic Al Kα source at 14.87 keV. Photoelectrons at 20 eV and 80 eV pass energy were detected with a multichannel detector. The spectra were fit by least-squares method to Voigt functions with Shirley baselines using CasaXPS. A MicroMeritics AccuPyc 1340 pycnometer was used to determine densities of synthesized chalcogels. Porosity measurements were performed using a MicroMeritics TriStar 3000 Porosimeter and the Brunauer—Emmett—Teller (BET) model and N_2 adsorption data at 77.4 K.

Electrochemical studies were initially carried out to optimize electrolyte and cycling conditions. In a Hohsen 316 CR2032 coin cell, cast films of MoS_x: SuperP®: polymeric binder (70:20:10 weight %) on carbon-coated Al foil were assembled with a Celgard 2400 polypropylene separator soaked in 60 μL of electrolyte, and 12 mm disc of Li foil. Binder used in composite electrode was carboxymethyl cellulose (CMC) and styrene-butadiene rubber (SBR). The electrolyte solution consisted of 1 M $LiPF_6$ in a 3:7 volume ratio of ethylene carbonate (EC) to ethylmethyl carbonate (EMC). Cells were cycled using a Bio-Logic VMP-3 between 1.0 V and 3.5 V at a rate of C/n (n = 40, 20, 10) in which n is the number of hours to transport 4 moles of Li^+. Cyclic voltammetry was done against Li/Li^+ counter electrode in a Hohsen 316 CR2032 coin cell configuration at 0.5 mV s^{-1}.

Ex-situ X-ray absorption fine structure spectroscopy was performed at the Advanced Photon Source 20-BM-B at Argonne National Laboratory. The powder samples were diluted with boron nitride and loaded into 1.5 mm Kapton capillary tubes for transmission measurements. The absorption was measured from Mo K-edge and calibrated to 20.36

keV[49] by normalization of the absorption energy from Mo foil. The E_0 value from Mo foil reference was used for all samples. Three scans were averaged for the reported absorption intensity using ATHENA, an open source package for spectroscopy analysis.[50] Analysis was done using ARTEMIS[50] between 1.5 Å and 4 Å. The k-range was analyzed from 3 Å to 12 Å^{-1} with Hanning windows and sills of 1 Å^{-1}.

Operando high-energy X-ray scattering data suitable for pair distribution function analysis have been collected at the PDF-dedicated beamline 11-ID-B at the Advanced Photon Source at Argonne National Laboratory. Rapid-acquisition total X-ray scattering measurements have been carried out using a Perkin-Elmer amorphous Si-based area detector at the X-ray wavelength of 0.2112 Å ($\approx$ 58 keV). The AMPIX cells[51] were assembled in an Ar glovebox with a MoS_x: graphite/Vulcan C (1:1): polytetrafluoroethylene (70:20:10 wt.%) cathode and 60 μL of 1 M $LiPF_6$ in EC/DMC (3:7 v/v) or 1 M LiTFSI in DOL/DME (1:1 v/v) soaked in glass fiber separator (Whatman) *vs.* Li/Li^+. The cells were cycled at $C/20$ between 1.0 V and 3.5 V or 1.7 V and 3.0 V at room temperature. NIST-traceable CeO_2 powder was used to calibrate experimental geometry of the measurements. Background contributions were collected using fully assembled AMPIX cell sans the MoS_x electrode. The 2D data were integrated using Fit2D.[52] Pair distribution functions (PDFs), $G(r)$, were calculated from the sine Fourier transform of the product $q(S(q) - 1)$ in which $S(q)$ is the structure factor. PDFs were generated with a q_{max} = 20 Å^{-1} using PDFgetX3.[53]

Results and discussion

Structural Characterization. The synthesis of MoS_x involves the oxidative coupling of the $(NH_4)_2MoS_4$ precursor with iodine.[44] The local structure consists of a Müller-type cluster[54] in which the Mo is in a +4 oxidation state and stabilized by a tricoordinated S atom (Figure 1). The presence of the Mo linkers in the random amorphous chalcogel network anchor the polysulfide chains. This network is shown in the TEM image shown in Fig-

ure 1a. The diffuse rings from SAED (Figure 1b) and wide-angle XRD show the lack of crystallinity with one diffuse peak centered at $2\theta = 21^\circ$ with a Cu $K\alpha$ source (Figure 1c). From Raman spectroscopy, vibrational modes of MoS_x chalcogel resemble that of amorphous MoS_3[55] (Figure 2a). As noted by Subrahmanyam *et al.*,[48] the amorphous MoS_x network does not consist of MoS_4 despite starting with the $(NH_4)_2MoS_4$ precursor. The Raman laser power was kept at a low power of 3.61 mW to prevent local oxidation of the chalcogel. However, the use of low power suppressed the weaker phonon modes from S–S stretching within the polysulfide chains between 500 cm^{-1} and 650 cm^{-1} seen in transition metal sulfides such as TiS_3,[56] ZrS_3,[57] and HfS_3.[58] SEM/EDS (Figure S1) and XPS (Figure 2b) suggest that the atomic ratio of S to Mo is 3.4:1. Density and porosity measurements show that the chalcogel has an average density of 2.7 g mL^{-1} and S_{BET} range between 6.2 and 30 m^2 g^{-1}.

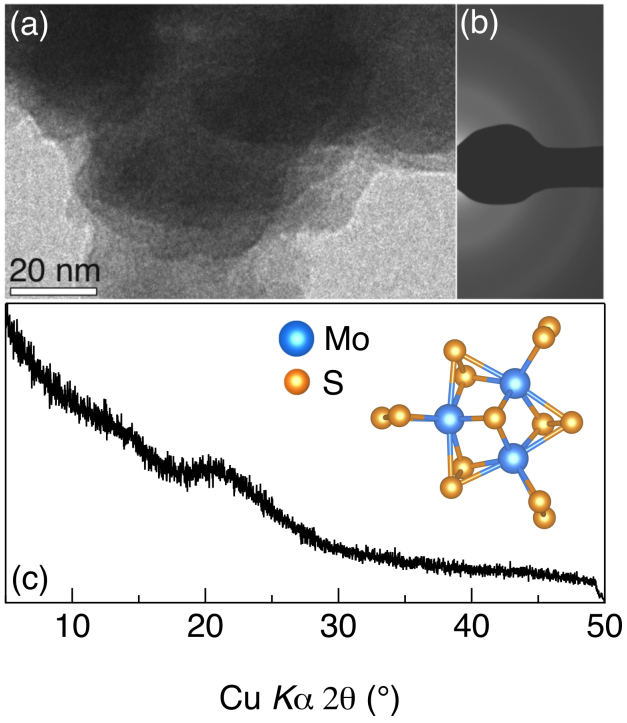

Figure 1: a) Transmission electron microscopy, (b) electron diffraction, and (c) X-ray diffraction capture the amorphous long-range structure of the MoS_x chalcogel with the local structure consisting of Müller[54]-type (Mo_3S_{13}) clusters.

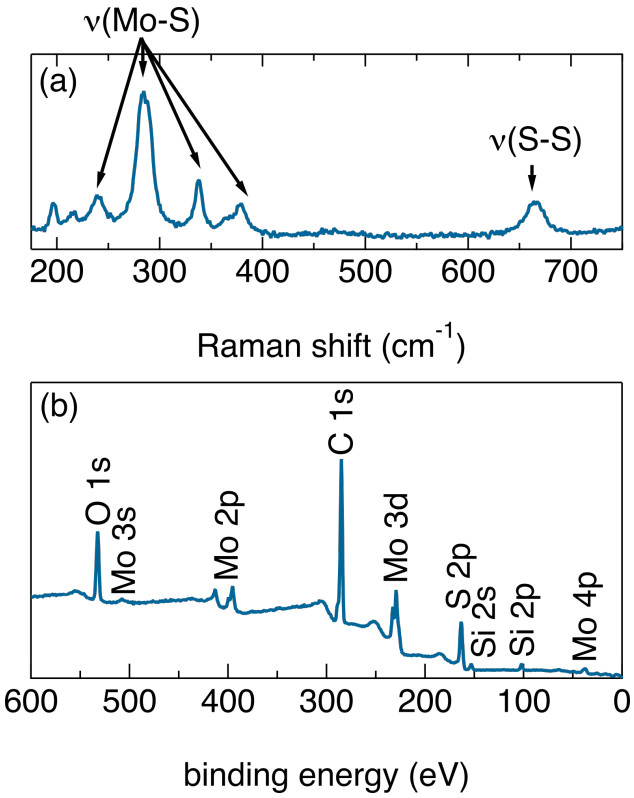

Figure 2: (a) Raman spectroscopy captures the Mo–S and S–S vibrational modes resembling that of MoS_3 in the as-prepared MoS_x powder. (b) XPS survey suggests a ratio of 3.4 S atoms to every Mo atom.

Electrochemical Characterization. Electrochemistry was studied *via* cyclic voltammetry (CV), electrochemical impedance spectroscopy (EIS), and galvanostatic cycling with potential limitation (GCPL) between 1.0 V and 3.5 V at room temperature (Figure 3a). The range was limited to 1.0 V to avoid most side reactions involving electrolyte decomposition on carbon. We assembled coin cells for CV and GCPL. MoS_x was cast into a film with Super P® and CMC/SBR binder in a ratio of 70:20:10 wt. $\%$ on carbon-coated Al current collector. A cyclic voltammetry sweep rate of 0.5 mV s^{-1} in EC:EMC exhibits an anodic peak at 2.3 V and cathodic peaks centered between 1.85 V and 1.74 V. Upon the 5th cycle, ΔV for the cathodic peak increased by 0.02 V. The cathodic peak changed from two peaks to one broader peak centered between 1.76 V and 1.65 V, which corresponds to the transformation of high-order to low-order polysulfide chains. The Nyquist plot of the cell (Figure 3b) can be fitted with a modified Randles equivalent-circuit model as depicted in the inset.[59–62] The impedance contribution from the carbonate-based electrolyte is 2.463 Ω. The high-frequency region resistances (R_2 = 240 Ω and R_3 = 602 Ω) are due to the roughness of the film arising from the amorphous morphology of the chalcogel. Additional fitted parameters for the constant phase elements are denoted in Table S1.

The gravimetric capacity upon the first discharge is 578 mAh g^{-1} based on the molar mass of MoS_4 (Figure 4a). This corresponds to a molar equivalence of 4.9 Li (Li:S = 1.44). The GCPL under constant current at a C-rate of $C/40$ exhibits sloping plateaus at 1.8 V upon discharge and 2.2 V upon charge in agreement with the single oxidation and reduction peaks observed in CV. The single plateau and absence of overcharging suggest that generation of dissolved lithium polysulfides (Li_nS_x) has been avoided.[63] Coulombic efficiency is maintained at $>95\%$ for 20 cycles. At faster C-rates of $C/20$ and $C/10$, the initial discharge capacity is decreased to 541.9 mAh g^{-1} and 460.7 mAh g^{-1} (Figure 4b). By the 2^{nd} cycle, the difference between the gravimetric capacities cycled at $C/20$ and $C/10$ are negligible. For $C/40$, the capacity retention is maintained at 83% upon the 10^{th} cycle and 60% upon the 30^{th} cycle, which is comparable to traditional Li–S batteries.[5] At

faster C-rates of $C/20$ and $C/10$, the capacity retention diverges after the 5^{th} cycle. At $C/20$, 63% of the capacity is retained upon the 20^{th} discharge. At $C/10$, the capacity drops more precipitously to 53% upon the 20^{th} discharge.

Formation of Intermediate Chemical Moieties. The intermediate chemical moieties Li_2S and MoS_2 are observed in *ex-situ* Raman spectroscopy with discharge to 1.8 V and 1.0 V, respectively (Figure 7). The characteristic T_{2g} mode for Li_2S is observed at 373 cm^{-1}.[64,65] With a 633 nm laser, the out-of-plane (A_{1g}) vibrational mode for the MoS_2 moiety is observed at 403 cm^{-1}.[66,67] At 1.0 V, the S–S vibrational modes are observed as weak bands at 568 cm^{-1} and 634 cm^{-1}. Upon charge, the MoS_2 A_{1g} mode at 403 cm^{-1} disappeared. At 2.2 V, there are broad sloping peaks 306 cm^{-1}, 322 cm^{-1}, and 353 cm^{-1} . The peak at 201 cm^{-1} was also observed at 1.8 V. Upon lithiation of MoS_2, Xiong *et al.*[67] have observed the emergence of this peak in tandem with the disappearance of the A_{1g} mode, which they have attributed this to the presence of Li^+ disrupting MoS_2 interlayer bonding. While we also observe the disappearance of the A_{1g} mode, the broad sloping peaks are not observed by Xiong *et al*. The set of three peaks could be attributed to Chevrel-based Mo_6S_8 moieties consisting of S^{2-} species.[68,69] The as-prepared chalcogel is formed again upon charging to 3.5 V. (Figure 2).

Role of inorganic linkers. The presence of the inorganic linkers is crucial for the high capacity retention, but are redox-inactive upon cycling. We use XPS to monitor the chemical states of Mo upon discharge to 1.8 V and 1.0 V as well as upon charge to 2.2 V and 3.5 V. The Mo $3d_{5/2}$ peaks are centered at 228.9 eV and are well separated from the $3d_{3/2}$ states at 3.1 eV higher binding energy. Due to the overlap of the S $2s$ states with Mo $3d_{5/2}$, we probed the S $2p$ states to elucidate the chemistry of S at various states of charge. The lower binding energy peaks, centered at 161.8 eV for $2p_{3/2}$ and 163.0 eV for $2p_{1/2}$, are attributed to terminal S atoms in the polysulfide chains, which are bonded to Mo linkers.[70,71] The covalently bonded bridging S atoms in the polysulfide

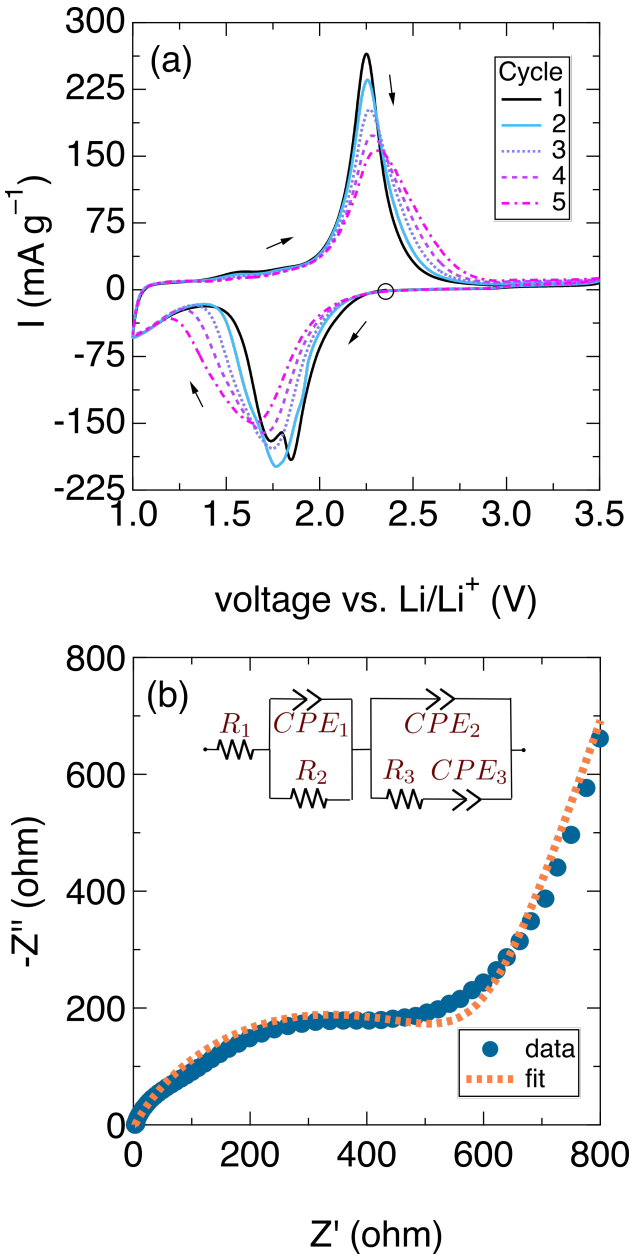

Figure 3: (a) Both cathodic and anodic peaks in the cyclic voltagram shift by less than 0.13 V with a sweep rate of 0.5 mV s^{-1} starting at the open circuit voltage (open circle) for a two-electrode configuration with MoS_x: Super P® as the electrode, 1 M $LiPF_6$ in EC:EMC (3:7 v/v) *vs.* Li/Li^+. (b) EIS of the prepared cell can be modeled with a modified Randles equivalent circuit (inset).

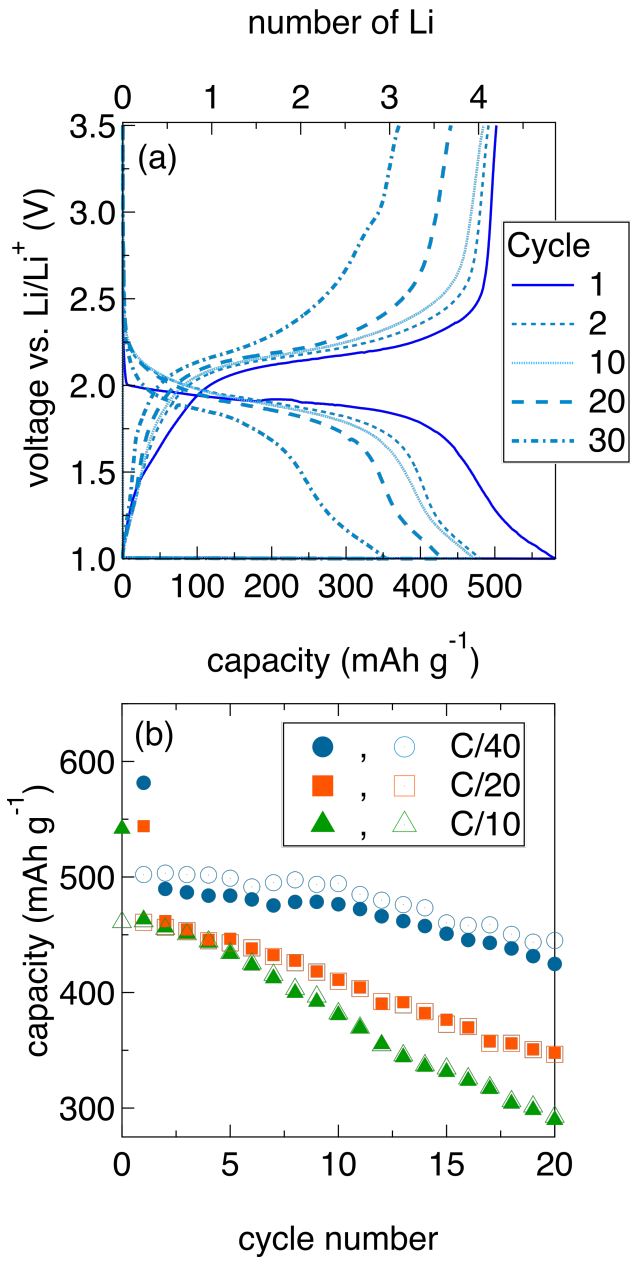

Figure 4: (a) Gravimetric capacity in galvanostatic cycling was normalized to the mass of MoS_4. (b) Capacity retention is maintained at 60% up to the 20^{th} cycle at C-rates of $C/40$, $C/20$, and $C/10$ upon discharge (filled) and charge (open).

chains are more strongly bound and thus register at higher binding energies. The distribution of these two chemical states of sulfur shifts as a function of state of charge without generation of elemental S or higher oxidation states of S. The decreased the signal-to-noise ratio at 1.0 V is attributed to the formation of the solid-electrolyte interphase. X-ray absorption fine structure (XAFS) was analyzed *via* fitting of the Fourier transform of the EXAFS equation, $\chi(k)$. Here, $\chi_j(k) = A_j(k)N_jF_j(k)S_0^2\sin(2kR_j + \phi_j(k))/kR_j^2$ and $A_j(k) = \exp\left(-2k^2\sigma_j^2\right)\exp\left(-2R_j/\lambda(k)\right)$. The calculated values are $F_j(k)$, the effective scattering amplitude, $\phi_j(k)$, the effective scattering phase shift, $\lambda(k)$, the mean free path. The parameters used for fitting the Mo_3S_{13} clusters were the Debye-Waller factor, σ^2, the energy shift, ΔE_0, and the change in the half-path length, Δr. Spectroscopy was done on samples collected at 1.8 V and 1.0 V upon discharge, 2.2 and 3.5 V upon charge, and the as-prepared MoS_x. Electronic excitation from the Mo $1s$ into the Mo $3d$/S $3p$ hybridized orbital probes the oxidation states of Mo in the as-prepared powder as compared with the intermediate species. The normalized absorption spectra for the discharged/charged states are indistinguishable from the as-prepared chalcogel. Using a Mo_3S_{13} (R-factor = 0.0081, χ^2 = 5,948.0, reduced χ^2 = 649.4) cluster model for the structure of the chemical moiety in the as-prepared chalcogel, absorption contributions from single scattering Mo–S and Mo–Mo paths are depicted in Figure 6. The prominent peak at r = 1.9 Å in Figure 6 is attributed to interactions with first and second-nearest S neighbors. The amorphous structure of the chalcogels is portrayed in the damped signal beyond 3 Å. The k^2-weighted $\chi(k)$ signal for the as-prepared sample is overlaid on the discharged and charged species in Figure 6. The overall amplitude reduction factor for Mo was fixed at 0.75. All the Mo–S correlations were treated equally, and the fitted parameters are summarized in Table 1.

Local Structure Evolution. Collecting *operando* PDFs allows for tracking the evolution of the local structure for materials that lack long-range ordering, which is particularly useful for chalcogels.[48,72–77] Here, PDFs of the MoS_x electrode cycled at constant current of 0.61

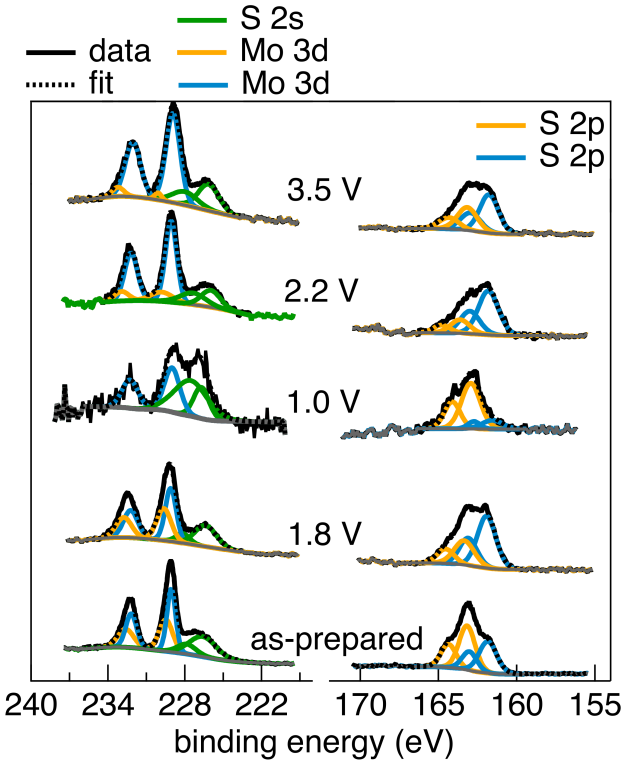

Figure 5: Mo 3d binding energy from *ex-situ* XPS of MoS_x electrodes remains constant upon discharge and charge. S 2p states are fitted to chemical states of terminal and bridging sulfur atoms. Upon discharge, there is an increase in the number of terminal S atoms as S–S bonds are broken. These broken links are formed again upon charge.

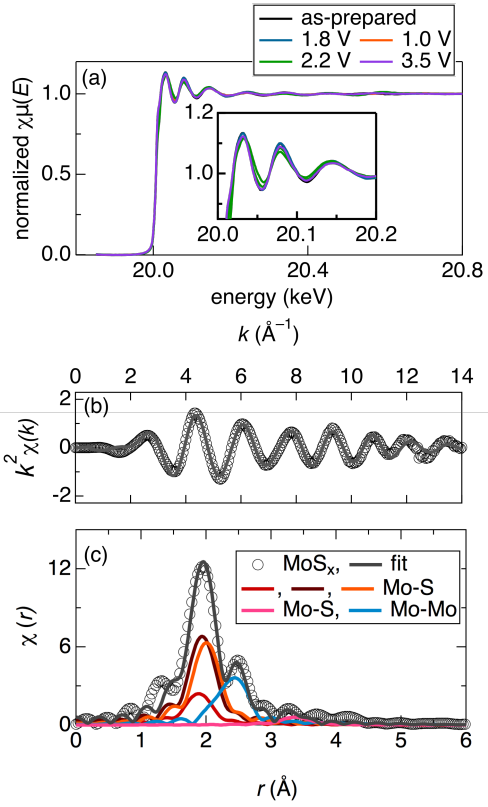

Figure 6: (a) Normalized absorption spectra of the as-prepared, discharged, and charged products are indistinguishable. (b) k^2-weighted EXAFS data for the as-prepared sample and its Fourier transform can be fit with a cluster model of Mo_3S_{13}, shown in Figure 1.

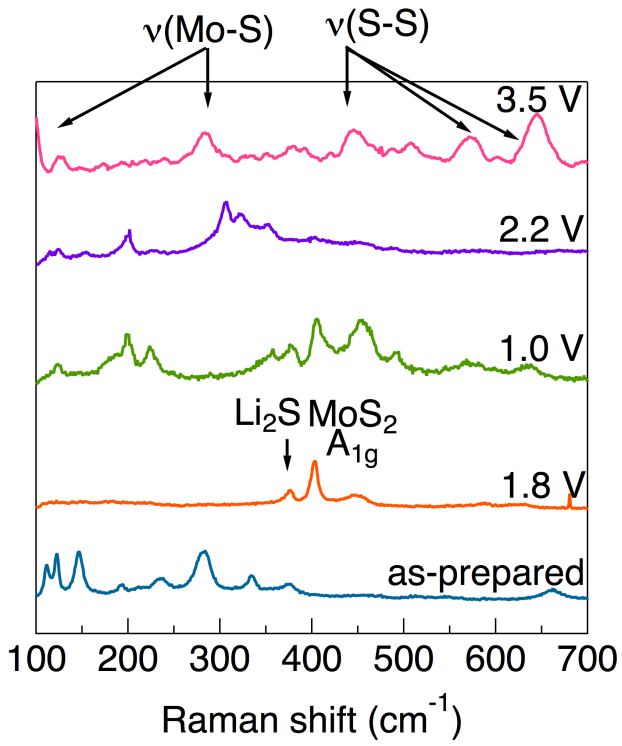

Figure 7: *Ex-situ* Raman spectroscopy of MoS_x electrodes at various states of discharge reveal intermediate species that include Li_2S and MoS_2 at 1.8 V and Mo_6S_8 at 1.0 V. Upon charge to 2.2 V, the Chevrel-based Mo_6S_8 moiety is formed. At 3.5 V, the normal modes of the MoS_x chalcogel $G(r)$are recovered.

Table 1: The Debye-Waller factors, absorption energy shifts, and bond distances for Mo–S and Mo–Mo nearest neighbors are fitted for the as-prepared chalcogel EXAFS spectrum for r between 1.5 Å and 4 Å. All Mo–S correlations are treated equally for fitting r and σ^2. A single ΔE_0 parameter (1.(1) eV) was fitted for both Mo–S and Mo–Mo correlations. The overall amplitude reduction factor for Mo was fixed at 0.75. Uncertainties for fitted parameters are noted in parentheses.

Correlation	σ^2 ($\times 10^{-3}$ Å^2)	r (Å)
Mo–S	3.57(4)	2.37(5), 2.42(5), 2.49(5), 3.87(5)
Mo–Mo	6.18(9)	2.76(9)

mA g^{-1} ($\approx C/16$) (Figure 8a) capture the Mo–S bonds centered at 2.45 Å in Figure 8b, which is unchanged upon discharge to 600.5 mAh g^{-1}. This peak subsumes contributions from Mo–S bonds in the Mo_3S_{13} cluster. In this local structure model, the Mo–S bond distances range from 2.37 Å for the tricoordinated S atom to 2.43 Å and 2.50 Å for the Mo bonded to each S_2^{2-}. The Mo–Mo bond starts at 2.8 Å for the as-prepared electrode, but increases marginally by 1% to 2.83 Å upon discharge and charge. The Mo–Mo bond distance is unchanged upon the second cycle of discharge and charge as well as the third discharge cycle. Anion redox is seen in the periodic change in intensity of the S–S bond at 2.07 Å. Figure 8c marks the potential values with dashed lines at the end of discharge (1.0 V) and charge (3.5 V) cycles with the mapped $G(r)$ peaked intensities as the contour levels. The PDF is damped beyond r = 3.5 Å(Figure S2) due to the armorphous structure of the chalcogel. The peak centers remain unchanged upon cycling, though the intensity of the S–S bond decreases upon discharge and increases upon charge. This suggests that S–S bonds are being broken and formed again (Scheme 1). The Mo–S and Mo–Mo correlations remain relatively constant upon discharge and charge.

We investigated the stability of the electrode in a smaller potential range, from 1.7 V to 3.0 V at 0.55 mA g^{-1} ($\approx C/18$) to understand the large decrease in gravimetric capacity after the first discharge. We observed a 20% loss in capacity retention upon the second discharge when the MoS_x electrode was cycled between 1.0 V and 3.5 V. The Coulombic efficiency of the first cycle was 74.8% with a 22.8% capacity loss from the

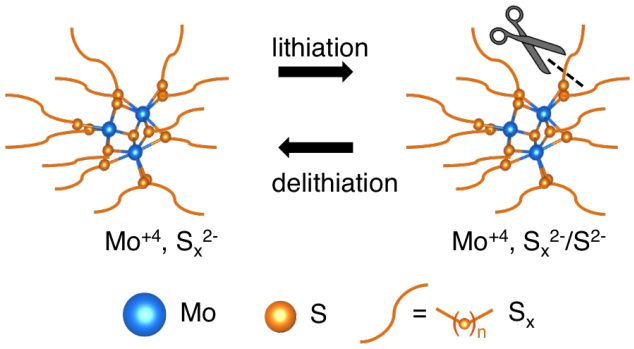

Scheme 1: Schematic of polysulfide chain scission in molybdenum chalcogels upon discharge/lithiation.

initial 429.7 mAh g^{-1} as shown in Figure S3a. Upon the second discharge, 77.1% of the initial capacity was retained. The PDFs collected *operando* for the electrode (MoS_x: graphite/Vulcan C: PTFE (70:20:10 wt. %)) in 1 M $LiPF_6$ in EC/DMC (3:7 v/v) in this potential window display similar changes in S–S peak intensity at 2.05 Å upon discharge and charge. While the Mo–S peak intensity does fade over the first three cycles, the Mo–Mo peak intensity remains constant (Figure S3b). The behavior of the third cycle was similar to that of the second cycle. Similar electrochemical behavior between the two potential windows suggest that there are irreversible chemical species formed upon the first discharge due to electrode–electrolyte side reactions. In contrast to the first cycle, Coulombic efficiency is maintained at 98.9% for the second and third cycles. One of the many strategies for increasing Li ion kinetics includes increasing the electrode surface area.[78,79] While benefits of increased porosity may initially result in increased capacity, subsequent cycling in materials such as mesoporous MnO have been reported to rapidly fade.[83] Therefore, we attribute the electrochemical reversibility and of these high-capacity chalcogel electrodes to their amorphous structure.

Cycling in ether–based electrolyte. MoS_x: Super P® was cycled with ether–based electrolytes traditionally used for Li–S batteries. In 1 M LiTFSI in a 1:1 by volume mixture of DOL/DME, the first discharge generated a capacity of 555.7 mAh g^{-1} corresponding to 4.7 moles of Li (Figure S4). There is a distinctive dissolution of polysulfide seen in a sharp

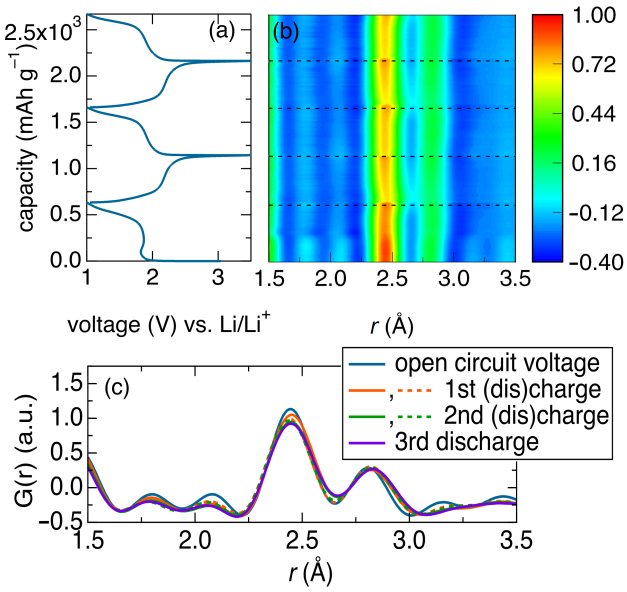

Figure 8: (a) Discharge and charge *vs.* Li/Li$^+$ at constant current of 0.61 mA g^{-1} of MoS$_x$ chalcogel in 1 M LiPF$_6$ in EC/DMC. (b) *Operando* PDFs capture the anion redox. (c) Selected PDFs at the end of each discharge (solid) and charge cycles (dashed) highlight the difference between the PDFs of the first discharge and subsequent cycles.

change in the polarization at 2.66 V upon the first charge. Upon a second charge, the overpotential increases to 2.77 V. By the fifth cycle, the overpotential peak disappeared, which suggests enhanced capability of the chalcogels to mitigate polysulfide shuttle effects. *Operando* PDFs collected for MoS$_x$: graphite/Vulcan C: PTFE (70:20:10 wt. %) in 1 M LiTFSI *vs.* Li/Li$^+$ captured similar electrochemical behavior with a change in polarization at 1.35 V upon discharge and 2.92 V upon charge during the first cycle (Figure 9a). In contrast to the *ex-situ* GCPL measurements, the dissolved species disappear by the second cycle. Due to various reactions, the capacity retention drastically decreased to 54.4% of the initial 1010.9 mAh g^{-1} upon the second discharge and 51.0 % upon the third discharge. The peaks centered at 2.08 Å, 2.42 Å, and 2.76 Å in Figure 9b correspond to S–S, Mo–S, and Mo–Mo bond distances as seen in the *operando* PDFs generated from cells with the carbonate-based electrolyte. Similarly, we observe a decrease in peak intensity upon discharge to 1.65 V and subsequently to 1.00 V and increase upon charge to 3.50 V. The electrochemical behavior and structural stability of chalcogel electrodes in ether–based elec-

trolytes are in contrast to the carbonate–based electrolytes. We speculate that the chalcogel undergoes a heterogeneous reaction with carbonate species resulting in organosulfur intermediates which are incompatible with carbonate–based electrolytes. Gao *et al.* performed *in-situ* XAFS to elucidate the polysulfide intermediates of a Li–S cell in ether–based (tetraethylene glycol dimethyl ether (TEGDME) and DOL/DME) and carbonate–based (propylene carbonate/EC/diethyl carbonate (PC/EC/DEC)) electrolytes.[80] They proposed two possible mechanisms upon cycling of Li–S batteries in PC/EC/DEC with catastrophic failure: (1) Thiolate methylation from a reaction with DEC and (2) alkali metal catalyzed thioether formation from a reaction with EC.[80–82] Irrespective of which mechanism may dominate, it is generally recognized that carbonate–based electrolytes are incompatible with the Li–S electrochemical couple. In ether–based electrolytes, polysulfide intermediates remained in solution and participated in the shuttle. Constructing a Li–S reference cell, we observed the almost instantaneous failure of the cell during the first discharge with linear carbonate electrolyte (Figure S5).

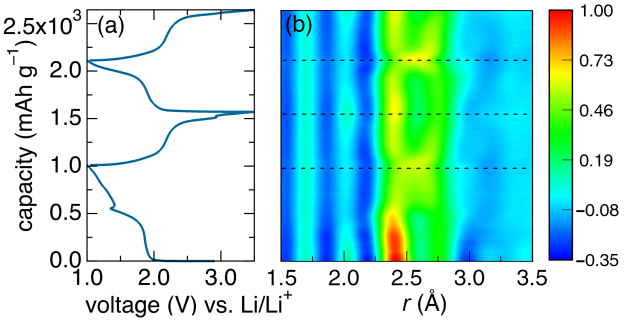

Figure 9: (a) Voltage curves cycled at 0.53 mA g^{-1} and (b) *operando* PDFs of MoS_x: graphite/Vulcan C: PTFE (70:20:10 wt.%) in 1 M LiTFSI in DOL/DME (1:1 v/v) *vs.* Li/Li^+.

Conclusion

We have demonstrated the use of MoS_x chalcogels as electrodes for high–capacity, anion–redox–driven electrochemical cells. The inorganically linked polysulfide chains transport 4.9 molar equivalents of Li ions corresponding to 578 mAh g^{-1} for $MoS_{3.4}$. Capacity re-

tention is high at 83% upon the 10^{th} cycle and 60% upon the 20^{th} cycle. These chalcogel electrodes are stable in both carbonate– and ether–based electrolytes, which allows for a larger parameter space for cell optimization. *Operando* PDFs demonstrate the transformations of the S–S bonds in the local structure model upon cycling. The local structure evolution reveals the Mo–S bonds remain intact in the carbonate–based electrolytes and prevent the polysulfide shuttle. We observe from *ex-situ* XPS and EXAFS in addition to PDF that the Mo linkers are redox–inactive. Instead, the electrochemistry is anion–driven. To increase gravimetric capacity, we propose similar chemistry can be applied to $3d$ transition metals when used as inorganic linkers in chalcogels.

Notes

The authors declare no competing financial interest.

Acknowledgement

We gratefully acknowledge the Southern California Electrochemical Energy Storage Alliance (SCEESA), supported by the California NanoSystems Institute (CNSI). Work at Northwestern University was supported by National Science Foundation Grant DMR-1410169. The use of shared experimental facilities of the Materials Research Laboratory: A National Science Foundation MRSEC supported by NSF DMR 1121053 is gratefully acknowledged. This research used resources of the Advanced Photon Source, a U.S. Department of Energy (DOE) Office of Science User Facility operated for the DOE Office of Science by Argonne National Laboratory under Contract No. DE-AC02-06CH11357. X-ray absorption experiments were performed at APS 20-BM-B under GUP-41555. X-ray scattering experiments were performed at APS 11-ID-B under GUP-46245. We thank AkzoNobel for providing a free sample of Ketjen Black EC-600JD, Mitsubishi Chemical for providing Sol-Rite™, and Coveris for providing carbon–coated Al foil. VDN is supported by the Uni-

versity of California President's Postdoctoral Fellowship and the University of California, Santa Barbara CNSI Elings Prize Fellowship. VDN thanks Professor Galen D. Stucky, Professor Anton Van der Ven, Dr. Thomas E. Mates, Paige Roberts, Jesse S. Ko, Jonathan S. J. Lau, and Ryan H. DeBlock for helpful discussions.

Supporting Information Available

Scanning electron micrographs of as-prepared MoS_x, fitted parameters for EIS of coin cell assembly in EC/EMC, *operando* pair distribution functions from total X-ray scattering of MoS_x: graphite/Vulcan C: PTFE in 1 M DOL/DME (1:1 v/v) (70:20:10 wt.$\%$) *vs.* Li/Li^+ between 1.0 V and 3.5 V, and *ex-situ* galvanostatic cycling of MoS_x: Super P® in 1 M EC/DMC (3:7 v/v) (70:20:10 wt. $\%$) *vs.* Li/Li^+ between 1.7 V and 3.0 V. This material is available free of charge via the Internet at `http://pubs.acs.org/`.

References

(1) Tarascon, J. M.; Armand, M. Issues and challenges facing rechargeable lithium batteries. *Nature* **2001**, *414*, 359–367.

(2) Cabana, J.; Monconduit, L.; Larcher, D.; Palacín, M. R. Beyond intercalation-based Li-ion batteries: The state of the art and challenges of electrode materials reacting through conversion reactions. *Adv. Mater.* **2010**, *22*, 170–192.

(3) Goodenough, J. B.; Park, K. S. The Li–ion rechargeable battery: A perspective. *J. Am. Chem. Soc.* **2013**, *135*, 1167–1176.

(4) Croguennec, L.; Palacín, M. R. Recent achievements on inorganic electrode materials for lithium-ion batteries. *J. Am. Chem. Soc.* **2015**, *137*, 3140–3156.

(5) Manthiram, A.; Fu, Y.; Chung, S.-H.; Zu, C.; Su, Y.-S. Rechargeable Lithium Sulfur Batteries. *Chem. Rev.* **2014**, *114*, 11751–87.

(6) Wang, H.; Yang, Y.; Liang, Y.; Robinson, J. T.; Li, Y.; Jackson, A.; Cui, Y.; Dai, H. Journals graphene–wrapped sulfur particles as a rechargeable lithium-sulfur battery cathode material with high capacity and cycling stability. *Nano Lett.* **2011**, *11*, 2644–2647.

(7) Zhou, W.; Yu, Y.; Chen, H.; DiSalvo, F. J.; Abruña, H. D. Yolk–shell structure of polyaniline–coated sulfur for lithium–sulfur batteries. *J. Am. Chem. Soc.* **2013**, 16736–16743.

(8) Ji, X.; Lee, K. T.; Nazar, L. F. A highly ordered nanostructured carbon–sulphur cathode for lithium–sulphur batteries. *Nat. Mater.* **2009**, *8*, 500–506.

(9) Demir-Cakan, R.; Morcrette, M.; Nouar, F.; Davoisne, C.; Devic, T.; Gonbeau, D.; Dominko, R.; Serre, C.; Ferey, G.; Tarascon, J.-M. Cathode composites for Li–S bat-

teries via the use of oxygenated porous architectures. *J. Am. Chem. Soc.* **2011**, *133*, 16154–16160.

(10) Ji, L.; Rao, M.; Zheng, H.; Zhang, L.; Li, Y.; Duan, W.; Guo, J.; Cairns, E. J.; Zhang, Y. Graphene oxide as a sulfur immobilizer in high performance lithium/sulfur cells. *J. Am. Chem. Soc.* **2011**, *133*, 18522–18525.

(11) Xin, S.; Gu, L.; Zhao, N. H.; Yin, Y. X.; Zhou, L. J.; Guo, Y. G.; Wan, L. J. Smaller sulfur molecules promise better lithium–sulfur batteries. *J. Am. Chem. Soc.* **2012**, *134*, 18510–18513.

(12) Wei, S.; Ma, L.; Hendrickson, K. E.; Tu, Z.; Archer, L. A. Metal–sulfur battery cathodes based on PAN-sulfur composites. *J. Am. Chem. Soc.* **2015**, *137*, 12143–12152.

(13) Al Salem, H.; Babu, G.; V. Rao, C.; Arava, L. M. R. Electrocatalytic polysulfide traps for controlling redox shuttle process of Li–S Batteries. *J. Am. Chem. Soc.* **2015**, *137*, 11542–11545.

(14) Apostolova, R. D.; Shembel', E. M.; Talyosef, I.; Grinblat, J.; Markovsky, B.; Aurbach, D. Study of electrolytic cobalt sulfide Co_9S_8 as an electrode material in lithium accumulator prototypes. *Russ. J. Electrochem.* **2009**, *45*, 311–319.

(15) Mikhaylik, Y. V.; Akridge, J. R. Polysulfide shuttle study in the Li/S battery system. *J. Electrochem. Soc.* **2004**, *151*, A1969–A1976.

(16) Choi, J. W.; Cheruvally, G.; Ahn, H. J.; Kim, K. W.; Ahn, J. H. Electrochemical characteristics of room temperature Li/FeS_2 batteries with natural pyrite cathode. *J. Power Sources* **2006**, *163*, 158–165.

(17) Dampier, F. W. Insoluble sulfide positive electrodes for organic electrolyte lithium secondary batteries. *J. Electrochem. Soc.* **1981**, *128*, 2501–2506.

(18) Bonino, F.; Lazzari, M.; Rivolta, B.; Scrosati, B. Electrochemical behavior of solid cathode materials in organic electrolyte lithium batteries: Copper sulfides. *J. Electrochem. Soc.* **1984**, *131*, 14980–1502.

(19) Jones, H. W.; Kovacs, P. E. Fe Mossbauer spectroscopy of reduced cathodes in the Li/FeS_2 battery system:evidence of superparamagnetism. *J. Phys. Chem.* **1990**, *94*, 832–836.

(20) Masset, P. J.; Guidotti, R. A. Thermal activated ("thermal") battery technology. Part IIIb. Sulfur and oxide-based cathode materials. *J. Power Sources* **2008**, *178*, 456–466.

(21) Jasinski, R.; Burrows, B. Cathodic discharge of nickel sulfide in a propylenecarbonate-$LiClO_4$ electrolyte. *J. Electrochem. Soc.* **1969**, *116*, 422.

(22) Julien, C. Lithium intercalated compounds charge transfer and related properties. *Mater. Sci. Eng. R Reports* **2003**, *40*, 47–102.

(23) Feng, C.; Ma, J.; Li, H.; Zeng, R.; Guo, Z.; Liu, H. Synthesis of molybdenum disulfide (MoS_2) for lithium ion battery applications. *Mater. Res. Bull.* **2009**, *44*, 1811–1815.

(24) Zhang, L.; Du, Y.; Ouyang, Y.; Xu, H.; Lu, X. G.; Liu, Y.; Kong, Y.; Wang, J. Atomic mobilities, diffusivities and simulation of diffusion growth in the Co–Si system. *Acta Mater.* **2008**, *56*, 3940–3950.

(25) Matsuyama, T.; Sakuda, A.; Hayashi, A.; Togawa, Y.; Mori, S.; Tatsumisago, M. Electrochemical properties of all-solid-state lithium batteries with amorphous titanium sulfide electrodes prepared by mechanical milling. *J. Solid State Electrochem.* **2013**, *17*, 2697–2701.

(26) Wu, H.-L.; Huff, L. A.; Gewirth, A. A. In situ Raman spectroscopy of sulfur speciation in lithium-sulfur batteries. *ACS Appl. Mater. Interfaces* **2015**, *7*, 1709–1719.

(27) Britto, S.; Leskes, M.; Hua, X.; Hébert, C.-A.; Shin, H. S.; Clarke, S.; Borkiewicz, O.; Chapman, K. W.; Seshadri, R.; Cho, J.; Grey, C. P. Multiple redox modes in the reversible lithiation of high-capacity, Peierls-distorted vanadium sulfide. *J. Am. Chem. Soc.* **2015**, *137*, 8499–8508.

(28) Kim, Y.; Park, K-s.; Song, S-h.; Han, J.; Goodenough, J. B. Access to M^{+3}/M^{+2} redox couples in layered $LiMS_2$ sulfides (M = Ti, V, Cr) as anodes for Li–ion battery. *J. Elec. Soc.* **2009**, *156*, A703-A708.

(29) Golodnitsky, D.; Peled, E. Pyrite as cathode insertion material in rechargeable lithium/composite polymer electrolyte batteries. *Electrochimica Acta* **1999**, *45*, 335–350.

(30) Débart, A.; Dupont, L.; Patrice, R.; Tarascon, J. M. Reactivity of transition metal (Co, Ni, Cu) sulphides versus lithium: The intriguing case of the copper sulphide. *Solid State Ionics* **2006**, *8*, 640–651.

(31) Bruce, P. G.; Scrosati, B.; Tarascon, J.-M. Nanomaterials for rechargeable lithium batteries. *Angew. Chemie Int. Ed.* **2008**, *47*, 2930–2946.

(32) Rolison, D. R.; Dunn, B. Electrically conductive oxide aerogels: new materials in electrochemistry. *J. Mater. Chem.* **2001**, *11*, 963–980.

(33) Dominko, R.; Arčon, D.; Mrzel, A.; Zorko, A.; Cevc, P.; Venturini, P.; Gaberscek, M.; Remskar, M.; Mihailovic, D. Dichalcogenide nanotube electrodes for Li–ion batteries. *Adv. Mater.* **2002**, *14*, 1531–1534.

(34) Ma, J.; Cui, C.; Hu, Z.; Xu, J.; Liu, H.; Li, X. Growth of MoS_2@C Nanobowls towards lithium–ion battery anode. *RSC Adv.* **2015**, *5*, 92506–92514.

(35) Hu, S.; Chen, W.; Zhou, J.; Yin, F.; Uchaker, E.; Zhang, Q.; Cao, G. Preparation

of carbon coated MoS_2 flower-like nanostructure with self-assembled nanosheets as high–performance lithium-ion battery anodes. *J. Mater. Chem. A* **2014**, *2*, 7862.

(36) Yang, L.; Wang, S.; Mao, J.; Deng, J.; Gao, Q.; Tang, Y.; Schmidt, O. G. Hierarchical MoS_2/polyaniline nanowires with excellent electrochemical performance for lithium–ion batteries. *Adv. Mater.* **2013**, *25*, 1180–1184.

(37) Yu, H.; Ma, C.; Ge, B.; Chen, Y.; Xu, Z.; Zhu, C.; Li, C.; Ouyang, Q.; Gao, P.; Li, J.; Sun, C.; Qi, L.; Wang, Y.; Li, F. Three-dimensional hierarchical architectures constructed by graphene/MoS_2 nanoflake arrays and their rapid charging/discharging properties as lithium-ion battery anodes. *Chem. - A Eur. J.* **2013**, *19*, 5818–5823.

(38) Zhao, C.; Kong, J.; Yao, X.; Tang, X.; Dong, Y.; Phua, S. L.; Lu, X. Thin MoS_2 nanoflakes encapsulated in carbon nanofibers as high–performance anodes for lithium–ion batteries. *ACS Appl. Mater. Interfaces* **2014**, *6*, 6383–6398.

(39) Wan, Z.; Shao, J.; Yun, J.; Zheng, H.; Gao, T.; Shen, M.; Qu, N.; Zheng, H. Core-shell structure of hierarchical quasi-hollow MoS_2 microspheres encapsulated porous carbon as stable anode for Li–ion batteries. *Small* **2014**, *10*, 4975–4981.

(40) Oh, Y.; Bag, S.; Malliakas, C. D.; Kanatzidis, M. G. Selective surfaces: High surface area zinc tin sulfide chalcogels. *Chem. Mater.* **2011**, *23*, 2447–2456.

(41) Islam, S. M.; Subrahmanyam, K. S.; Malliakas, C. D.; Kanatzidis, M. G. One-dimensional molybdenum thiochlorides and their use in high surface area MoS_x. *Chem. Mater.* **2014**, *26*, 5151–5160.

(42) Bag, S.; Gaudette, A. F.; Bussell, M. E.; Kanatzidis, M. G. Spongy chalcogels of non-platinum metals act as effective hydrodesulfurization catalysts. *Nat. Chem.* **2009**, *1*, 217–224.

(43) Shafaei-Fallah, M.; Rothenberger, A.; Katsoulidis, A. P.; He, J.; Malliakas, C. D.; Kanatzidis, M. G. Extraordinary selectivity of $CoMo_3S_{13}$ chalcogel for C_2H_6 and CO_2 adsorption. *Adv. Mater.* **2011**, *23*, 4857–4860.

(44) Subrahmanyam, K. S.; Sarma, D.; Malliakas, C. D.; Polychronopoulou, K.; Riley, B. J.; Pierce, D. a.; Chun, J.; Kanatzidis, M. G. Chalcogenide aerogels as sorbents for radioactive iodine. *Chem. Mater.* **2015**, *27*, 2619–2626.

(45) Oh, Y.; Morris, C. D.; Kanatzidis, M. G. Polysulfide chalcogels with ion-exchange properties and highly efficient mercury vapor sorption. *J. Am. Chem. Soc.* **2012**, *134*, 14604–14608.

(46) Shim, Y.; Young, R. M.; Douvalis, A. P.; Dyar, S. M.; Yuhas, B. D.; Bakas, T.; Wasielewski, M. R.; Kanatzidis, M. G. Enhanced photochemical hydrogen evolution from the Fe_4S_4-based biomimetic chalcogels containing M^{2+} (M = Pt, Zn, Co, Ni, Sn) centers. *J. Am. Chem. Soc.* **2014**, *136*, 13371–13380.

(47) Staszak-Jirkovský, J.; Malliakas, C. D. D.; Lopes, P. P. P.; Danilovic, N.; Kota, S. S.; Chang, K.-C.; Genorio, B.; Strmcnik, D.; Stamenkovic, V. R.; Kanatzidis, M. G.; Markovic, N. M. Design of active and stable Co–Mo–S_x chalcogels as pH-universal catalysts for the hydrogen evolution reaction. *Nat. Mater.* **2016**, *15*, 197–204.

(48) Subrahmanyam, K. S.; Malliakas, C. D.; Sarma, D.; Armatas, G. S.; Wu, J.; Kanatzidis, M. G. Ion-exchangeable molybdenum-sulfide porous chalcogel: Gas adsorption and capture of iodine and mercury. *J. Am. Chem. Soc.* **2015**, *137*, 1394313948.

(49) Kraft, S.; Stümpel, J.; Becker, P.; Kuetgens, U. High resolution X-ray absorption spectroscopy with absolute energy calibration for the determination of absorption edge energies. *Rev. Sci. Instrum.* **1996**, *67*, 681–687.

(50) Ravel, B.; Newville, M. ATHENA, ARTEMIS, HEPHAESTUS: data analysis for X-ray absorption spectroscopy using IFEFFIT. *J. Synchrotron Radiat.* **2005**, *12*, 537–541.

(51) Borkiewicz, O. J.; Shyam, B.; Wiaderek, K. M.; Kurtz, C.; Chupas, P. J.; Chapman, K. W. The AMPIX electrochemical cell: A versatile apparatus for in situ X-ray scattering and spectroscopic measurements. *J. Appl. Crystallogr.* **2012**, *45*, 1261–1269.

(52) Hammersley, A. P. FIT2D: A multi-purpose data reduction, analysis and visualization program. *J. Appl. Crystallogr.* **2016**, *49*, 646–652.

(53) Juhás, P.; Davis, T.; Farrow, C. L.; Billinge, S. J. L. PDFgetX3: A rapid and highly automatable program for processing powder diffraction data into total scattering pair distribution functions. *J. Appl. Crystallogr.* **2013**, *46*, 560–566.

(54) Müller, A.; Sarkar, S.; Gopal Bhattacharyya, R.; Pohl, S.; Dartmann, M. Directed synthesis of $[Mo_3S_{13}]^{2-}$, an isolated cluster containing sulfur atoms in three different states of bonding. *Angew. Chemie* **1978**, *90*, 535.

(55) Chang, C. H.; Chan, S. S. Infrared and Raman studies of amorphous MoS_3 and poorly crystalline MoS_2. *J. Catal.* **1981**, *72*, 139–148.

(56) Galliardt, D. W.; Nieveen, W. R.; Kirby, R. D. Lattice properties of the linear chain compound TiS_3. *Solid State Commun.* **1980**, *34*, 37–39.

(57) Harbec, J.Y. and Cavellin, D. C. and Jandl, S. Raman spectra and crystal symmetry of ZrS_3. *Phys. Stat. Sol.* **1979**, *96*, K117–K120.

(58) Deville Cavellin, C.; Jandl, S. Raman spectra of HfS_3. *Solid State Commun.* **1980**, *33*, 813–816.

(59) Holzapfel, M.; Martinent, A.; Alloin, F.; Le Gorrec, B.; Yazami, R.; Montella, C. First

lithiation and charge/discharge cycles of graphite materials, investigated by electrochemical impedance spectroscopy. *J. Electroanal. Chem.* **2003**, *546*, 41–50.

(60) Pajkossy, T. Impedance spectroscopy at interfaces of metals and aqueous solutions – surface roughness, CPE and related issues. *Solid State Ionics* **2005**, *176*, 1997–2003.

(61) Hirschorn, B.; Orazem, M. E.; Tribollet, B.; Vivier, V.; Frateur, I.; Musiani, M. Constant–Phase–Element behavior caused by resistivity distributions in films: I. Theory. *J. Electrochem. Soc.* **2010**, *157*, C452–C457.

(62) Deng, Z.; Zhang, Z.; Lai, Y.; Liu, J.; Li, J.; Liu, Y. Electrochemical impedance spectroscopy study of a lithium/sulfur battery: Modeling and analysis of capacity fading. *J. Electrochem. Soc.* **2013**, *160*, A553–A558.

(63) See, K. A.; Leskes, M.; Griffin, J. M.; Britto, S.; Matthews, P. D.; Emly, A.; Ven, A. V. D.; Wright, D. S.; Morris, A. J.; Grey, C. P.; Seshadri, R. Ab initio structure search and in situ ^{7}Li NMR studies of discharge products in the Li-S battery system. *J. Am. Chem. Soc.* **2014**, *136*, 16368–16377.

(64) Bertheville, B.; Bill, H.; Hagemann, H. Experimental Raman scattering investigation of phonon anharmonicity effects in Li_2S. *J. Phys. Condens. Matter* **1999**, *10*, 2155–2169.

(65) Grzechnik, A.; Vegas, A.; Syassen, K.; Loa, I.; Hanfland, M.; Jansen, M. Reversible antifluorite to anticotunnite phase transition in Li_2S at high pressures. *J. Solid State Chem.* **2000**, *154*, 603–611.

(66) Li, H.; Zhang, Q.; Yap, C. C. R.; Tay, B. K.; Edwin, T. H. T.; Olivier, A.; Baillargeat, D. From bulk to monolayer MoS_2: Evolution of Raman scattering. *Adv. Funct. Mater.* **2012**, *22*, 1385–1390.

(67) Xiong, F.; Wang, H.; Liu, X.; Sun, J.; Brongersma, M.; Pop, E.; Cui, Y. Li Intercalation in MoS_2: In situ observation of its dynamics and tuning optical and electrical properties. *Nano Lett.* **2015**, *15*, 6777–6784.

(68) McCarley, R. E.; Hilsenbeck, S. J.; Xie, X. Amorphous precursors for low-temperature preparation of Chevrel phases $M_xMo_6S_8$ and their tungsten analogues. *J. Solid State Chem.* **1995**, *117*, 269–274.

(69) Hilsenbeck, S. J.; McCarley, R. E.; Goldman, A. I. Thermal deligation of $Mo_6S_8L_6$ cluster Complexes. EXAFS and other spectroscopic techniques support retention of the Mo_6S_8 cluster unit up to 500°C. *Chem. Mater.* **1995**, *7*, 499–506.

(70) Smart, R. S. C.; Skinner, W. M.; Gerson, A. R. XPS of sulphide mineral surfaces: Metal-deficient, polysulphides, defects and elemental sulphur. *Surf. Interface Anal.* **1999**, *28*, 101–105.

(71) Pang, S. H.; Schoenbaum, C. A.; Schwartz, D. K.; Medlin, J. W. Effects of thiol modifiers on the kinetics of furfural hydrogenation over Pd catalysts. *ACS Catal.* **2014**, *4*, 3123–3131.

(72) Egami, T.; Billinge, S. J. L. *Underneath the Bragg peaks: Structural analysis of complex materials*, 2nd ed.; Elsevier: Amsterdam, 2003.

(73) Doan-Nguyen, V. V. T.; Kimber, S. A. J.; Pontoni, D.; Reifsnyder Hickey, D.; Diroll, B. T.; Yang, X.; Miglierini, M.; Murray, C. B.; Billinge, S. J. L. Bulk metallic glass-like scattering signal in small metallic nanoparticles. *ACS Nano* **2014**, *8*, 6163–6170.

(74) Doan-Nguyen, V. V. T.; Zhang, S.; Trigg, E. B.; Agarwal, R.; Li, J.; Su, D.; Winey, K. I.; Murray, C. B. Synthesis and Xray characterization of cobalt phosphide (Co_2P) nanorods for the oxygen reduction reaction. *ACS Nano* **2015**, *9*, 8108–8115.

(75) Hua, X.; Robert, R.; Du, L.-S.; Wiaderek, K. M.; Leskes, M.; Chapman, K. W.; Chupas, P. J.; Grey, C. P. Comprehensive study of the CuF_2 conversion reaction mechanism in a lithium ion battery. *J. Phys. Chem. C* **2014**, *118*, 15169–15184.

(76) Hua, X.; Liu, Z.; Bruce, P. G.; Grey, C. P. The morphology of TiO_2(B) nanoparticles. *J. Am. Chem. Soc.* **2015**, *2*, 13612–13623.

(77) Allan, P. K.; Griffin, J. M.; Darwiche, A.; Borkiewicz, O. J.; Wiaderek, K. M.; Chapman, K. W.; Morris, A. J.; Chupas, P. J.; Monconduit, L.; Grey, C. P. Tracking sodium-antimonide phase transformations in sodium-ion anodes: Insights from operando pair distribution function analysis and solid-state NMR Spectroscopy. *J. Am. Chem. Soc.* **2016**, *138*, 2352–2365.

(78) Tarascon, J.-M.; Poizot, P.; Laruelle, S.; Grugeon, S.; Dupont, L. Nano-sized transition-metal oxides as negative-electrode materials for lithium-ion batteries. *Nature* **2000**, *407*, 496–499.

(79) Shi, Y.; Guo, B.; Corr, S. A.; Shi, Q.; Hu, Y.-S.; Heier, K. R.; Chen, L.; Seshadri, R.; Stucky, G. D. Ordered mesoporous metallic MoO_2 materials with highly reversible lithium storage capacity. *Nano Lett.* **2009**, *9*, 4215–4220.

(80) Gao, J.; Lowe, M. A.; Kiya, K.; Abruña, H. D. Effects of liquid electrolytes on the charge–discharge performance of rechargeable lithium/sulfur batteries: Electrochemical and in situ X–ray absorption spectroscopic studies. *J. Phys. Chem. C* **2011**, *115*, 25132-25137.

(81) Ono, Y. Catalysis in the production and reactions of dimethyl carbonate, an environmentally benign building block. *Appl. Cat. A: General* **1997**, *155*, 133-166.

(82) Clements, J. H. Reactive applications of cyclic alkylene carbonates. *Ind. & Eng. Chem. Res.* **2003**, *42*, 663-674.

(83) Butala, M. M.; Danks, K. R.; Lumley, M. A.; Zhou, S.; Melot, B. C.; Seshadri, R. MnO conversion in Li-ion batteries: In situ studies and the role of mesostructuring. *ACS Appl. Mater. Interfaces* **2016**, *8*, 6496–6503.

Graphical TOC Entry

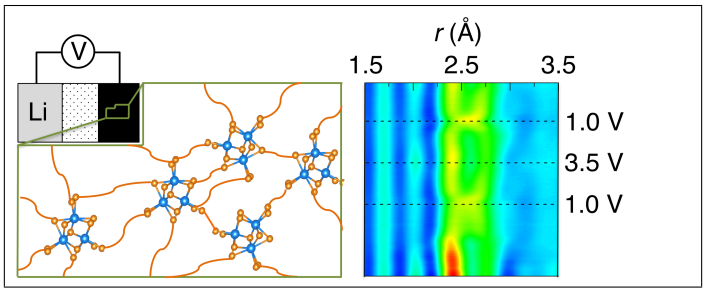

Molybdenum Polysulfide Chalcogels as High−Capacity, Anion−Redox−Driven Electrode Materials for Li-ion Batteries Supporting Information

Vicky V. T. Doan-Nguyen,[*,†,‡] Kota S. Subrahmanyam,[¶] Megan M. Butala,[§] Jeffrey A. Gerbec,[‖] Saiful M. Islam,[¶] Katherine N. Kanipe,[⊥] Catrina E. Wilson,[⊥] Mahalingam Balasubramanian,[#] Kamila M. Wiaderek,[#] Olaf J. Borkiewicz,[#] Karena W. Chapman,[#] Peter J. Chupas,[#] Martin Moskovits,[⊥] Bruce S. Dunn,[@] Mercouri G. Kanatzidis,[¶] and Ram Seshadri[‡,§,⊥]

†*California NanoSystems Institute, University of California, Santa Barbara, CA 93106*

‡*Materials Research Laboratory, University of California, Santa Barbara, CA 93106*

¶*Department of Chemistry, Northwestern University, Evanston, IL 60208*

§*Materials Department, University of California, Santa Barbara, CA 93106*

‖*Mitsubishi Chemical Center for Advanced Materials, Santa Barbara, CA 93106*

⊥*Department of Chemistry and Biochemistry, University of California, Santa Barbara, CA 93106*

#*X-ray Science Division, Advanced Photon Source, Argonne National Laboratory, Argonne, IL 60439*

@*Department of Materials Science and Engineering, University of California, Los Angeles, CA 90095*

E-mail: vdn@mrl.ucsb.edu

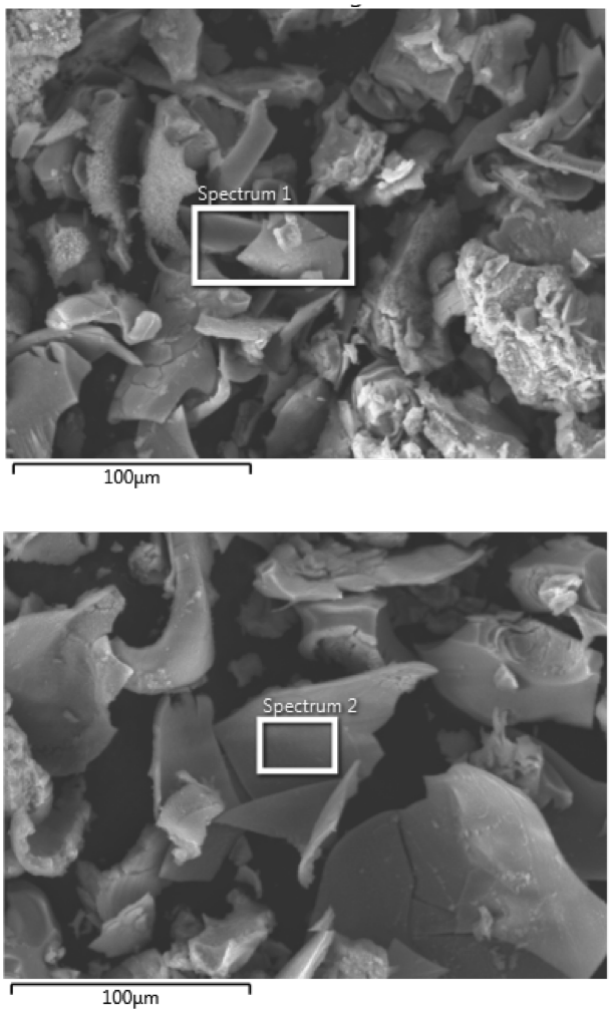

Figure S 1: Elemental analysis of the highlighted regions confirms the atomic ratio of 3.37 S to 1 Mo for the area denoted as "Spectrum 1" and 3.34 S to 1 Mo for the area denoted as "Spectrum 2".

Table S 1: EIS for MoS_x coin cell in which the impedance for the constant phase element is defined as Z = $\frac{1}{Q(i\omega)^{\alpha}}$ and χ^2= 1.165. R_1 is the high frequency intercept with the $Z^{'}$ axis. The high-frequency ($>$ 1 kHz) and low-frequency regions are modeled using three constant phase elements to capture the surface contact resistance (roughness) within the electrode (R_2 $\|$ CPE_1) as well as the charge-transfer resistance between the electrode and the electrolyte (R_3 $\|$ CPE_2), respectively. The diffusion of ions within the electrode is represented by the Warburg impedance (CPE_3).

R_1 (Ω)	R_2 (Ω)	R_3 (Ω)	Q_1 (F $s^{(\alpha_1-1)}cm^{-2}$)	α_1	Q_2 (F $s^{(\alpha_2-1)}cm^{-2}$)	α_2	Q_3 (F $s^{(\alpha_3-1)}cm^{-2}$)	α_3
2.463	240	602	5.818×10^{-4}	1	6.497×10^{-4}	0.7029	5.02×10^{-5}	0.6749

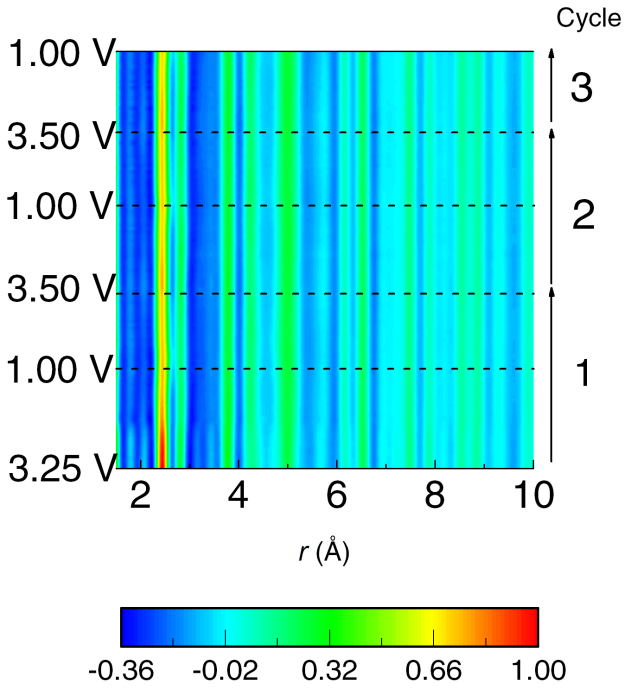

Figure S 2: *Operando* PDFs of MoS_x: graphite/Vulcan C in 1 M $LiPF_6$ in EC/DMC (3:7 v/v) *vs.* Li/Li^+ cycled with a constant applied current of 0.61 mA g^{-1} between 1.0 V and 3.5 V.

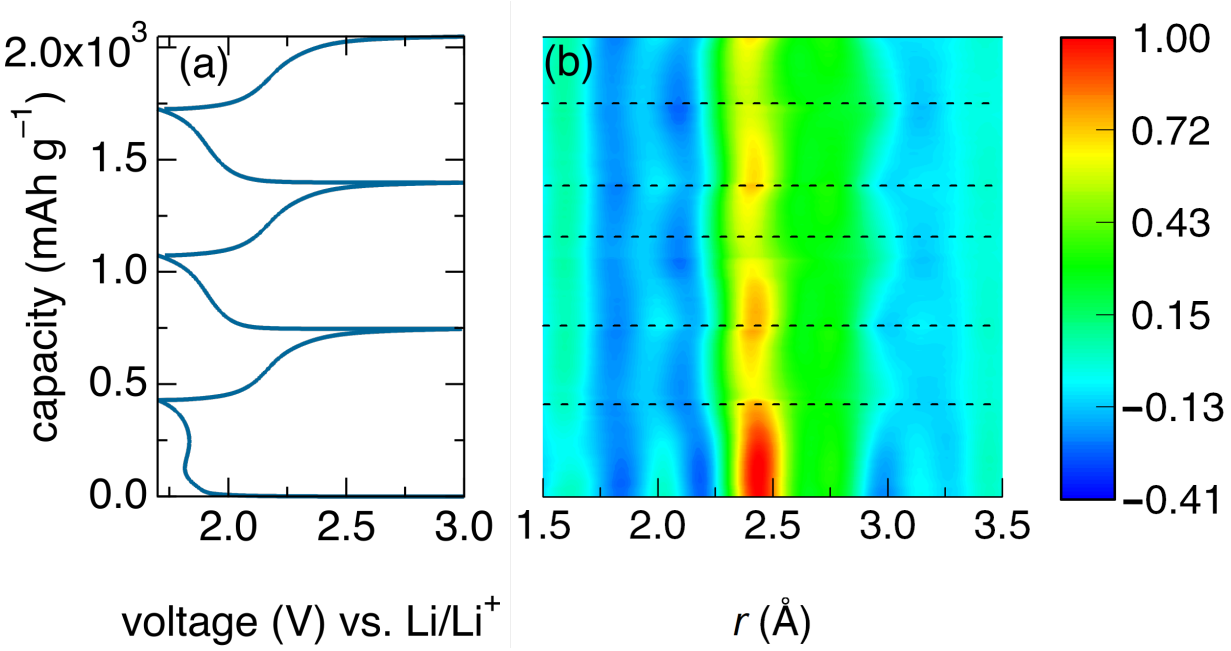

Figure S 3: *Operando* PDFs of MoS_x: graphite/Vulcan C in 1 M $LiPF_6$ in EC/DMC (3:7 v/v) *vs.* Li/Li^+ cycled with a constant applied current of 0.55 mA g^{-1} between 1.7 V and 3.0 V.

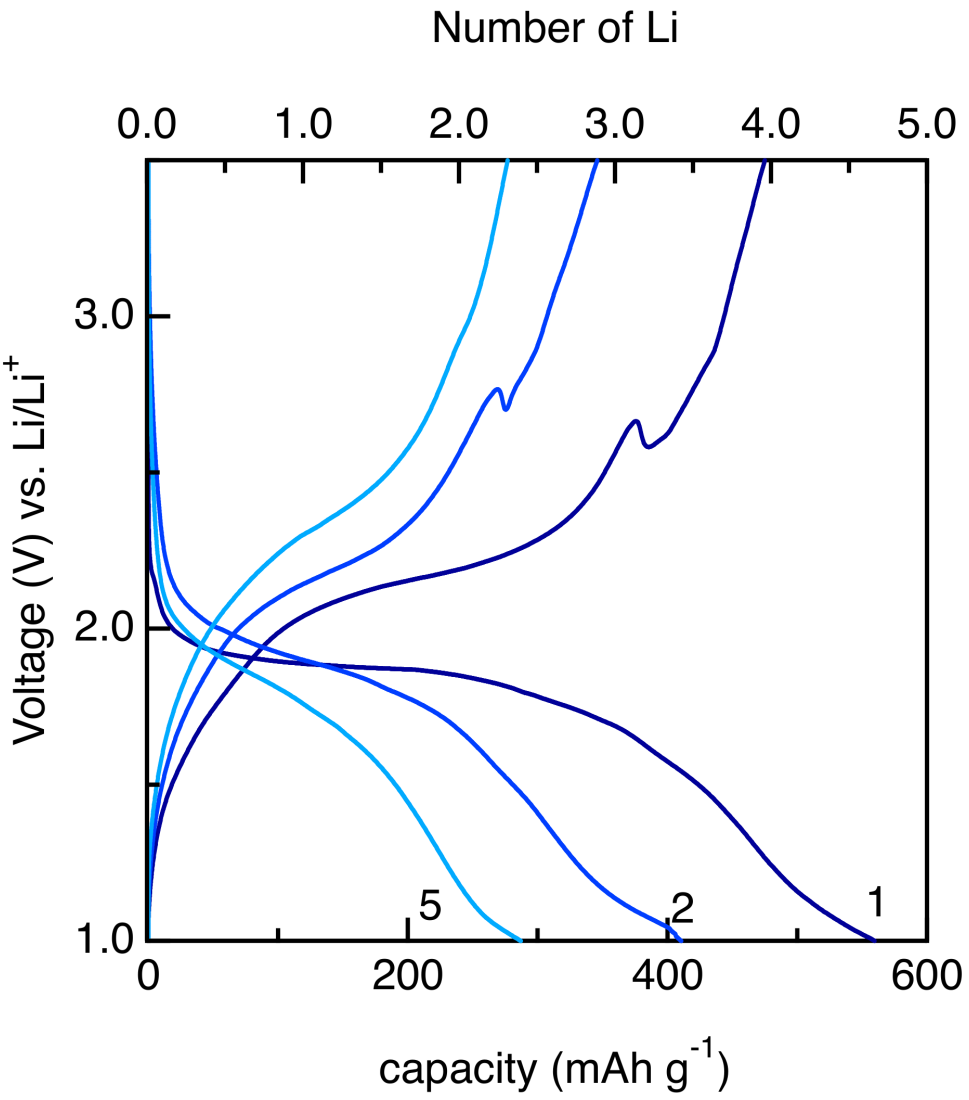

Figure S 4: Galvanostatic cycling of MoS_x:Super P® (85:15 wt.%) as the cathode, 1 M LiTFSI in DOL/DME (1:1 v/v) *vs.* Li/Li^+ at $C/20$ upon the 1^{st}, 2^{nd}, and 5^{th} cycles.

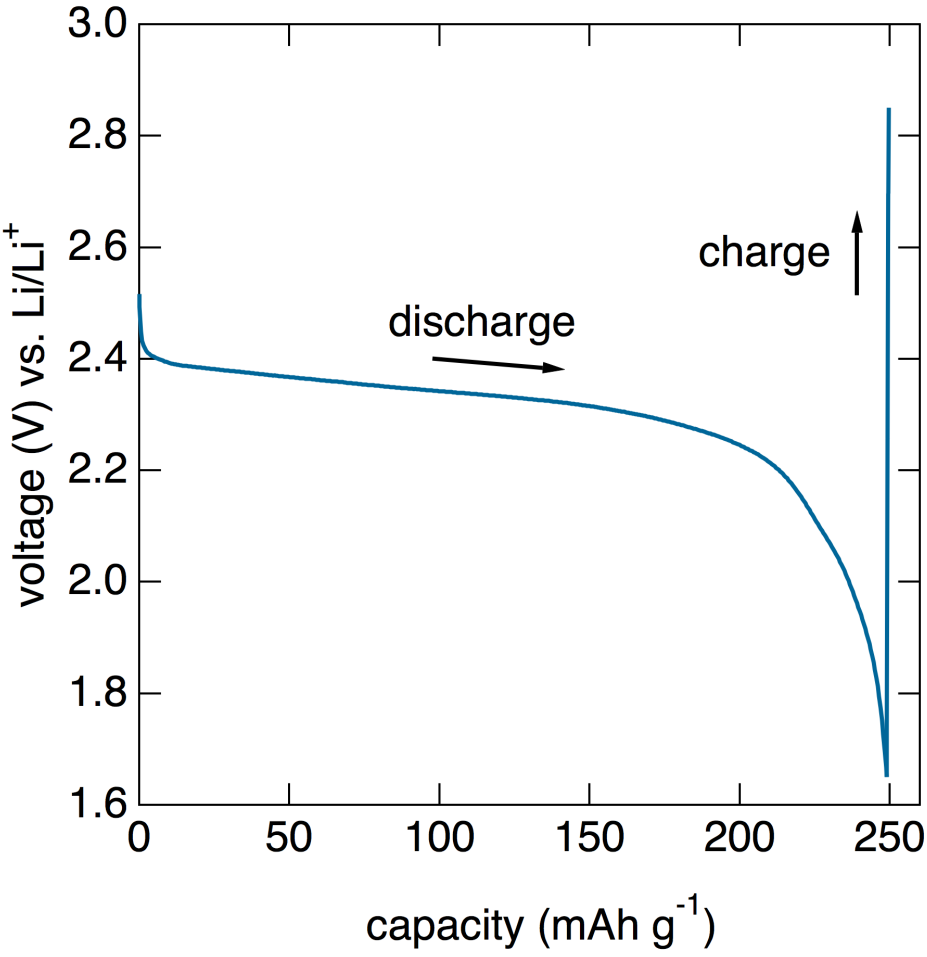

Figure S 5: First discharge and charge of a reference Li–S cell with S:carbon:binder (55:35:10 wt.%) as the cathode, 1 M $LiPF_6$ in EC/DMC (1:1 v/v) *vs.* Li/Li^+ at 0.25 mA g^{-1} show incompatibility of sulfur cathode in carbonate–based electrolyte.